

## Supporting Information for Publication (SI)

### Neutron Diffraction Study of a Sintered Iron Electrode In Operando

Bernhard M.H. Weninger<sup>a</sup>, Michel A. Thijs<sup>b</sup>, Jeroen A.C. Nijman<sup>c</sup>, Lambert van Eijck<sup>b</sup> and  
Fokko M. Mulder<sup>\*,a</sup>

<sup>a</sup>) Materials for Energy Conversion and Storage (MECS), Delft University of Technology, 2629 HZ Delft, Netherlands

<sup>b</sup>) Neutron and Positron Methods in Materials (NPM2), Delft University of Technology, 2629 JB Delft, Netherlands

<sup>c</sup>) Independent researcher

\*Corresponding author E-mail: [F.M.Mulder@tudelft.nl](mailto:F.M.Mulder@tudelft.nl)

# Index

Index	Page
<u>Extended Experimental Section</u>	S3
Iron Characterization	S3
Figure S1	
Electrode Production	S4
Figure S2	
Executed Electrochemical Program	S5
Figure S3	
Table S1	
Iron Oxide/Hydroxide Simulation	S7
Figure S4	
Table S2	
Rietveld Refinement of the Most Discharged Stage	S9
Figure S5	
Table S3	
Calculation of Volumetric Hydrogen Content	S10
Table S4	
Table S5	
Table S6	
<u>Results</u>	S12
Start of Discharging from a Charged Electrode	S12
Figure S6	
Steady Gradients for the First Discharge Plateau	S13
Table S7	
Charging from the First Discharge Plateau	S13
Figure S7	
Table S8	
The Second Iron Discharge-Plateau	S15
Table S9	
Table S10	
Correlation between Phase Precipitation and Detector Counts	S16
<u>Discussion</u>	S17
Correlation Fractional Phase Changes - Detector Counts	S17
Figure S8	
<u>References</u>	S19

## Extended Experimental Section

### Iron Characterization.

Reduced metallic iron powder was produced through reduction of hematite in a flow-through reactor. A weight loss of 30% can be expected for full conversion from hematite ( $\text{Fe}_2\text{O}_3$ ) to iron. The measured weight loss of 30% points indicates full conversion. The reduced powder used for the production of the electrode was characterized by neutron diffraction. Figure S1 shows the measured diffraction pattern together with the refined data for iron. Only peaks related to iron are visible, confirming full conversion to iron.

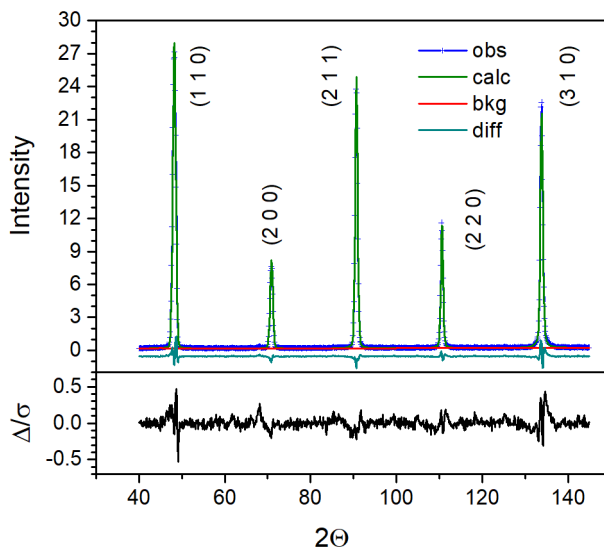


**Figure S1.** Top: Observed intensities for the reduced iron powder (obs), together with calculated intensities (calc), background (bkg) and difference (diff) curve. Bottom: Difference curve divided by the estimated standard deviation for the data points (GSAS II output).

## Extended Experimental Section

### Electrode Production

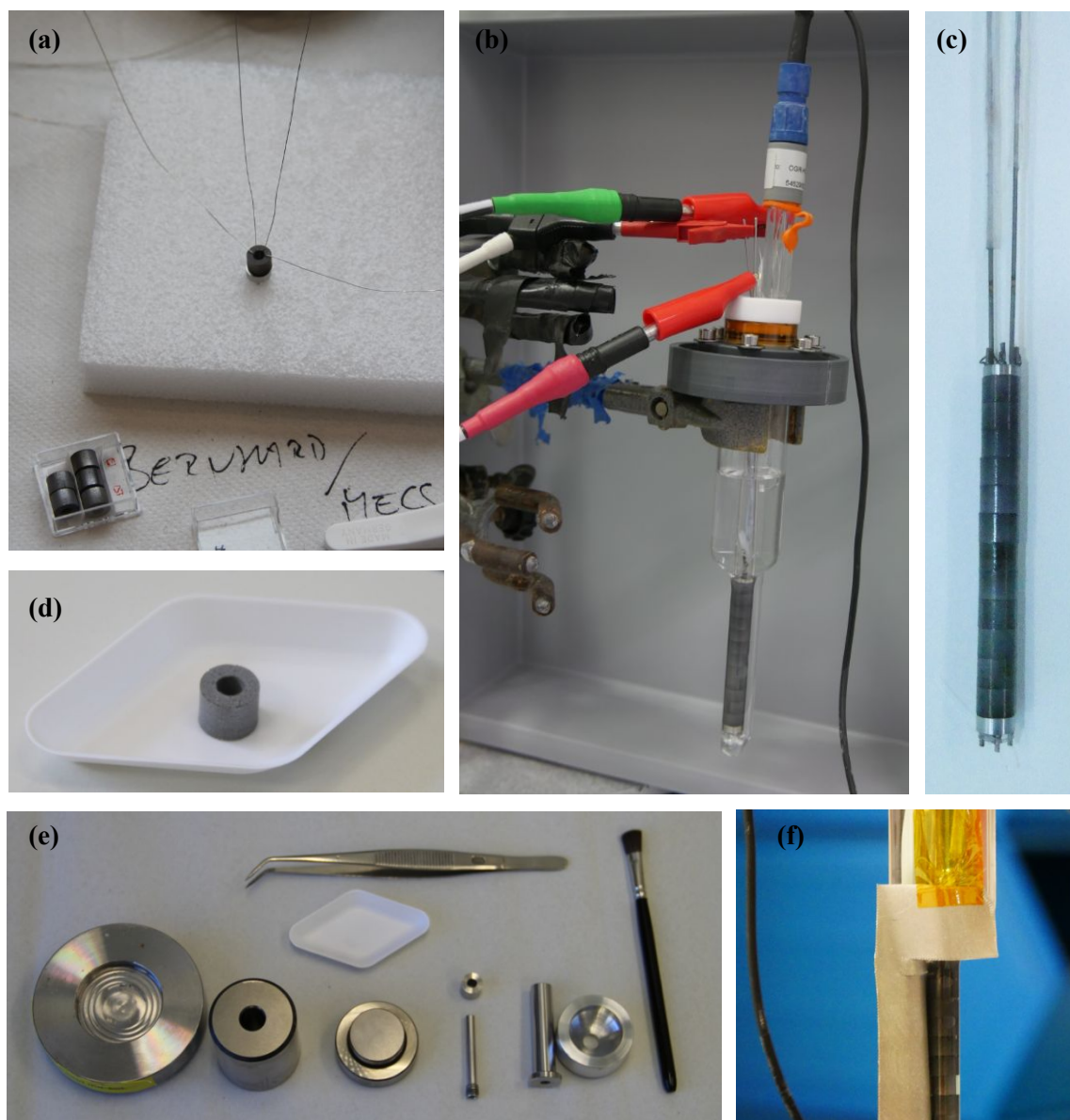


**Figure S2.** Electrode production and preliminary electrode testing: (a) Assembly of the tubular electrode stack. Four thin Ni wires (0.25mm thick) in the center hold the electrode together. They are fixed at both end elements enclosing the twelve individual electrodes. (b) Preliminary testing of the electrode. The setup comprises the tubular iron electrode, the centered nickel wire counter electrode and a Hg/HgO reference electrode which senses the headspace. A capillary at the backside connects the headspace with the bottom of the cell to provide electrolyte. (c) Assembled iron electrode after testing. (d) Tubular electrode after pressing. Inner diameter 3.5 mm, outer diameter 8.0 mm. Sintering causes the electrode to shrink to the reported inner diameters of 3.23 mm and outer diameter of 7.53 mm. (e) 8 mm die set for pressing the electrodes with an extra insert for the tubular shape. (f) Shielding of the capillary, the end elements (stainless steel) and parts of the sample holder during the measurement with Cd foil to prevent unnecessary reflections and background.



## Extended Experimental Section

### Executed Electrochemical Program

This study contains four electrochemical cycles of discharging and then recharging. In the first two cycles we investigate the phase changes for the first iron discharge plateau. In the first cycle we used a moderate discharge rate of 200 mA. In the second cycle we used a 50% higher discharge rate of 300 mA. Sluggish discharge characteristics are a downside of iron electrodes. In cycles three and four we investigate the phase changes for extended discharging. Our aim is to identify the iron phase of the second iron discharge plateau. Session one (measurements 0-167) consists of: Cycle 1, Cycle 2 and Cycle 3 to a partial recharge to a capacity of 0.323 Ah/g<sub>Fe</sub>. Session 2 (measurements 192-266) includes the Cycle 4 discharge from a discharge capacity of 0.156 Ah/g<sub>Fe</sub> to 0.423 Ah/g<sub>Fe</sub> and the partial recharge to 0.262 Ah/g<sub>Fe</sub>. The third session (measurement 281-284) consists of the recharge for cycle four from 0.406 Ah/g<sub>Fe</sub> to 0.454 Ah/g<sub>Fe</sub>. Figure S3 shows a timeline of the performed test together with the neutron diffraction measurements. Table S1 provides an overview of the executed electrochemical program including all rates and capacities. All (re)charges were programmed to slightly overcharge the electrode at a rate of 300 mA. A charge rate of 300 mA is equivalent to 46.6 mA/g<sub>Fe</sub> or to a current density of 46.3 mA/cm<sup>2</sup> at the inner circumference of the tube iron electrode. The corresponding current density at the outer circumference of the counter electrode is twice as high, 92.6 mA/cm<sup>2</sup>.

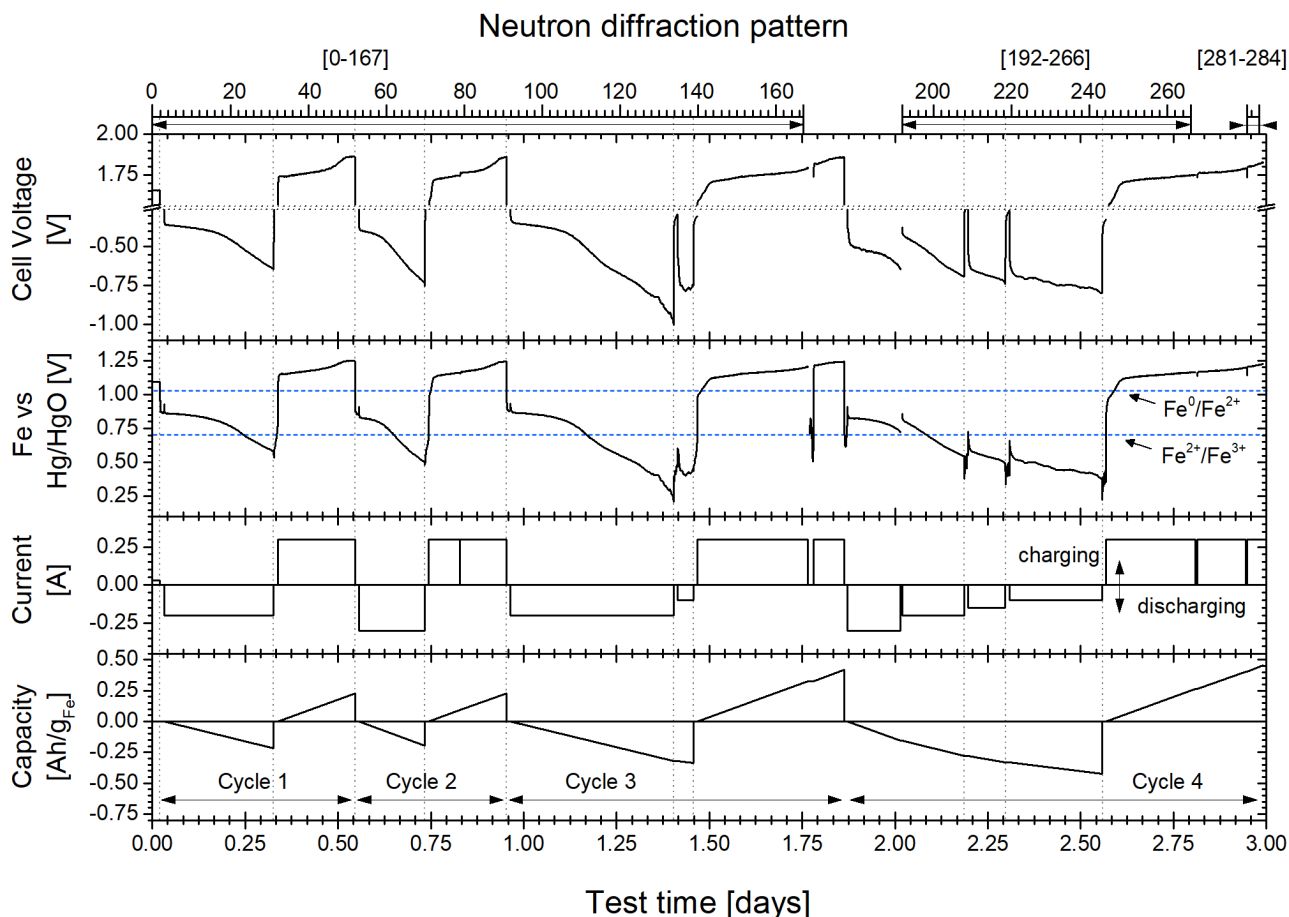


**Figure S3.** Executed test program with programmed test current [A] (negative sign discharging, positive sign charging) together with observed cell voltage [V], the voltage of the iron electrode relative to a Hg/HgO reference electrode [V] with inverted sign, and the calculated (dis)charge capacity [Ah/g<sub>Fe</sub>]. Top: Numbering of the neutron diffraction measurements; the tick marks indicate the start of a measurement.

## Extended Experimental Section

**Table S1. Executed Electrochemical Program**

	Discharge rate	Discharge to capacity	Charge capacity	Session
Cycle 1	200 mA	0.214 Ah/g <sub>Fe</sub>	0.228 Ah/g <sub>Fe</sub>	1
Cycle 2	300 mA	0.192 Ah/g <sub>Fe</sub>	0.228 Ah/g <sub>Fe</sub>	1
Cycle 3	200 mA 100 mA	0.320 Ah/g <sub>Fe</sub> 0.335 Ah/g <sub>Fe</sub>	0.419 Ah/g <sub>Fe</sub>	1: until a charge capacity of 0.323 Ah/g <sub>Fe</sub>
Cycle 4	300 mA 200 mA 150 mA 100 mA	0.156 Ah/g <sub>Fe</sub> 0.277 Ah/g <sub>Fe</sub> 0.332 Ah/g <sub>Fe</sub> 0.423 Ah/g <sub>Fe</sub>	0.454 Ah/g <sub>Fe</sub>	2, starting with discharging at discharge capacity of 0.156 Ah/g <sub>Fe</sub> to charging up to a capacity of 0.262 Ah/g <sub>Fe</sub> . 3: recharging from 0.406 Ah/g <sub>Fe</sub> to 0.454 Ah/g <sub>Fe</sub>

## Extended Experimental Section

### Iron Oxide/Hydroxide Simulation

Figure S4 shows on top the observed measurement data for the most discharged sample and below simulations for various iron oxides and (oxy)hydroxides. The simulations were performed with GSAS II.<sup>1</sup> Table S2 depicts the used CIF files with their structural data used for the simulation, downloaded from the Crystallographic database<sup>2-7</sup>. Figure S4 illustrates that none of the simulated iron oxides has a characteristic pattern the matches the main three peaks identified for the second iron discharge plateau.

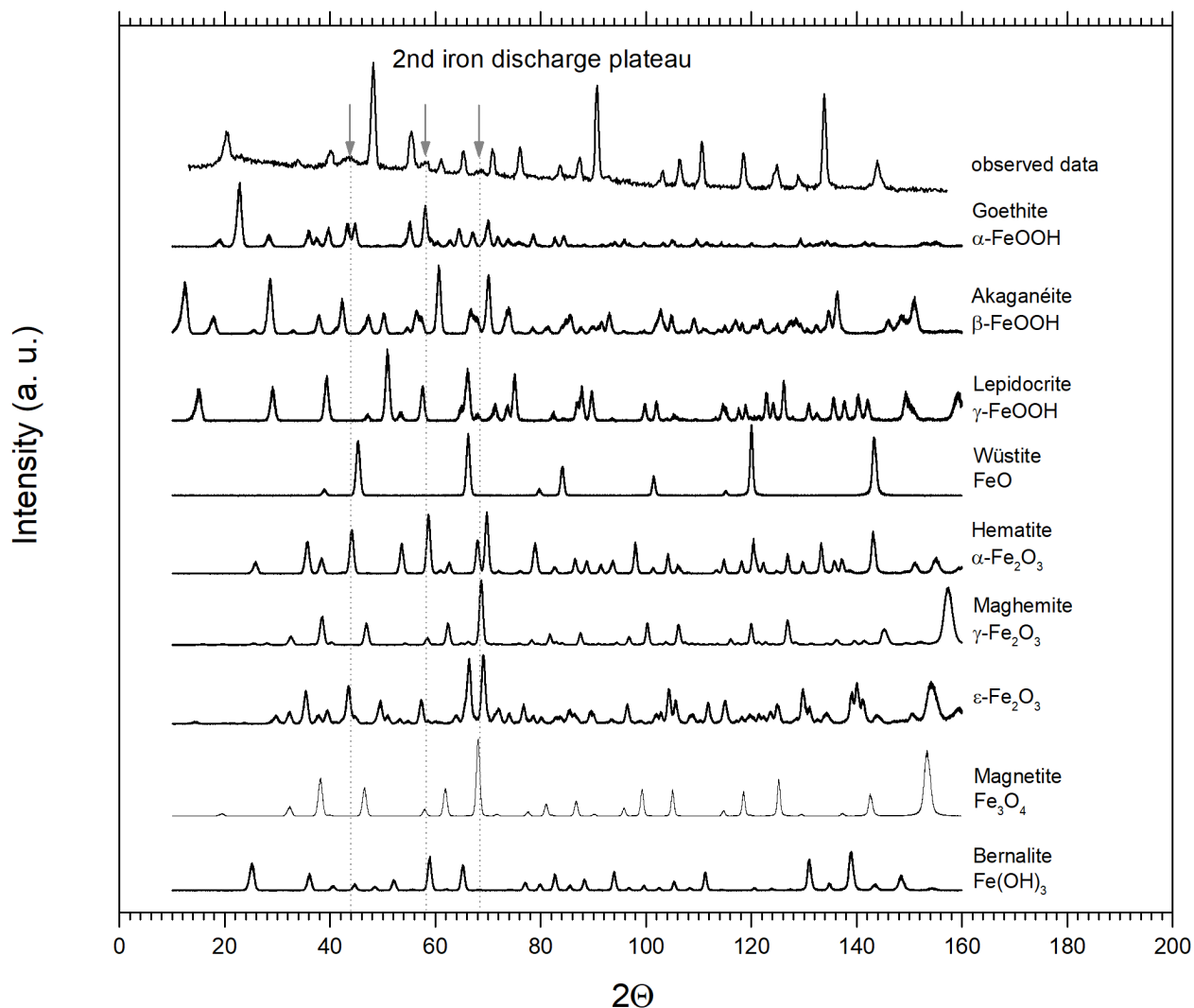


**Figure S4.** Top: Observed diffraction data for the most discharged state. Below: In descending order simulated neutron diffraction data for:  $\alpha, \beta, \gamma$ -FeOOH, FeO,  $\alpha, \gamma, \epsilon$ -Fe<sub>2</sub>O<sub>3</sub>, Fe<sub>3</sub>O<sub>4</sub>, and Fe(OH)<sub>3</sub>;



## Extended Experimental Section

**Table S2 CIF-Files and Structure Data for Simulated Iron Oxides and (Oxy)hydroxides**

Compound	CIF file	Structure
Magnetite, $\text{Fe}_3\text{O}_4$	9002316	F d 3 m; a = 8.3965 Å;
Goethite, $\alpha\text{-FeOOH}$	9002158	P n m a; a = 9.9134 Å, b = 3.0128 Å, c = 4.58 Å
Akaganéite, $\beta\text{-FeOOH}$	1531989	I 1 2/m 1; a = 10.587 Å, b = 3.0311 Å, c = 10.515 Å
Lepidocrocite, $\gamma\text{-FeOOH}$	9009154	B b m m; a = 12.4 Å, b = 3.87 Å, c = 3.06 Å
Wüstite, FeO	1011198	F m -3 m; a = 4.303 Å
Hematite, $\alpha\text{-Fe}_2\text{O}_3$	2101167	R -3 c; a = 5.0355 Å; c = 13.7471 Å
Maghemite, $\gamma\text{-Fe}_2\text{O}_3$	9012692	P 4 <sub>3</sub> 2 <sub>1</sub> 2; a = b = 8.3396 Å, c = 8.322 Å
$\epsilon\text{-Fe}_2\text{O}_3$	4002383	P n a 2 <sub>1</sub> ; a = 5.085 Å, b = 8.774 Å, c = 9.468 Å
Bernalite, $\text{Fe}(\text{OH})_3$	9016365	I m m m; a = 7.544 Å, b = 7.560 Å, c = 7.558 Å

## Extended Experimental Section

### Rietveld Refinement of the Most Discharged Stage

Figure S5 shows on top the observed measurement data for the most discharged sample and below simulations for the identified and refined phases: iron, iron hydroxide, iron oxyhydroxide, and nickel. Table S3 provides the refined structural parameters belonging to the Rietveld refinement. The data residuals wR result in 0.910% on 1366 observations, and  $\chi^2 = 1.6$ .

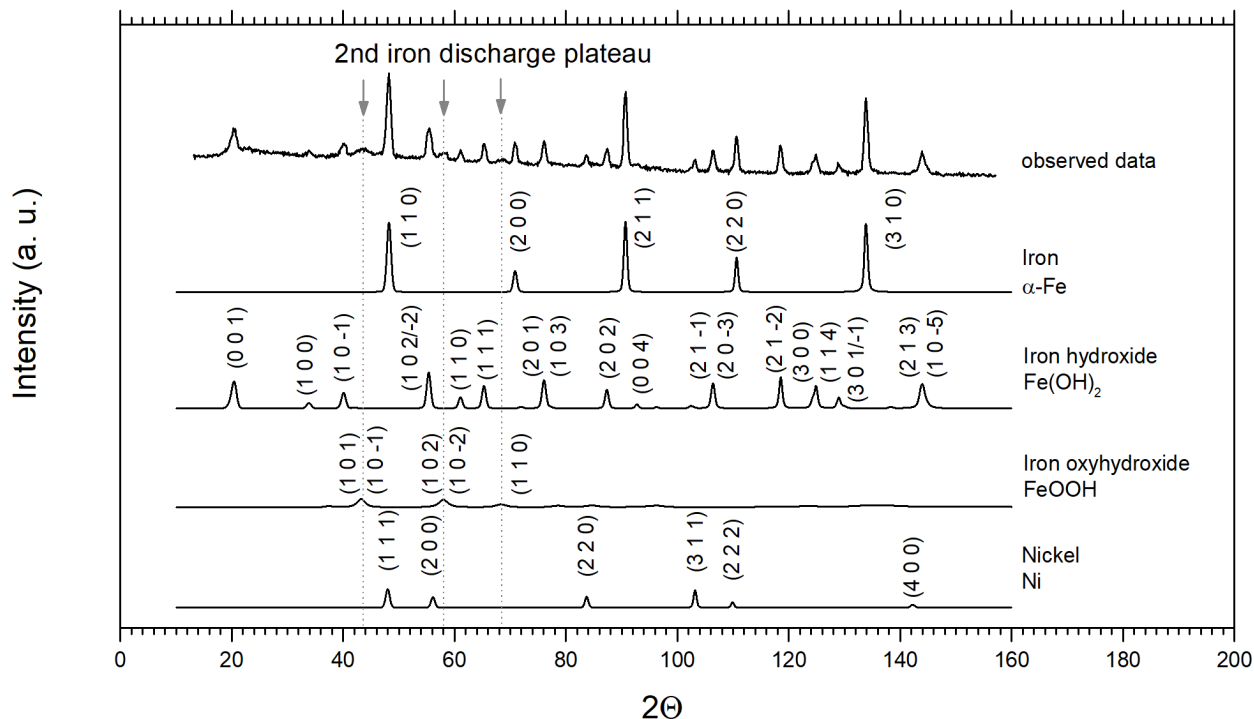


**Figure S5.** Top: Observed diffraction data for the most discharged state. Below: Simulated diffraction pattern for the identified compounds iron, iron hydroxide, iron oxyhydroxide, and nickel of the refined structure.

**Table S3. Structural Parameters of the Refined Phases**

Compound	Iron	Iron hydroxide	Iron oxyhydroxide	Nickel
space group	Im-3m no. 229	P-3m1 no. 164	P-3m1 no. 164	Fm-3m no. 225
lattice parameters	a = 2.866 Å	a = 3.267 Å c = 4.601 Å	a = 2.956 Å c = 4.590 Å	a = 3.526 Å
atom site in Wyckoff notation*	Fe: 2a (0,0,0)	Fe: 1a (0,0,0) O: 2d (1/3,2/3,0.223) H: 2d (1/3,2/3,0.423)	Fe <sub>1</sub> : 1a (0,0,0) Fe <sub>2</sub> : 1b (0,0,1/2) O: 2d (1/3,2/3,1/4) H <sub>1</sub> : 2d (1/3,2/3,0.46) H <sub>2</sub> : 2d (1/3,2/3,0.04) H <sub>3</sub> : 2d (1/3,2/3,-1/8) H <sub>3</sub> : 2d (1/3,2/3,5/8)	Ni: 4a (0,0,0)
occupancy	Fe: 1.000	Fe: 1.000 O: 1.000 H: 0.881	Fe <sub>1</sub> , Fe <sub>2</sub> : 0.5 O: 1.000 H <sub>1</sub> , H <sub>2</sub> , H <sub>3</sub> , H <sub>4</sub> : 0.125	Ni: 1.000
size (μm)	0.175	0.1	0.0226	1
micostrain	821	3000	42148	2000
Unweighted phase residuals (GSASII output)	RF <sup>2</sup> : 4.482% RF: 1.560%	RF <sup>2</sup> : 4.387% RF: 1.972%	RF <sup>2</sup> : 9.232% RF: 3.571%	RF <sup>2</sup> : 8.785% RF: 3.024%

\*) Wyckoff positions are retrieved from Bilbao Crystallographic server<sup>8</sup>

## Extended Experimental Section

### Calculation of Volumetric Hydrogen Content.

The following section provides calculations concerning the expected hydrogen content. First the hydrogen content of compounds is calculated, see table S4. With changing the composition changes. The composition change causes the porosity to change and with it the volume available for electrolyte.

**Table S4. Calculated Volumetric Hydrogen Densities.**

Compound	Density [g/cm <sup>3</sup> ]	Molar weight [g/mol]	Compound content [mol/cm <sup>3</sup> ]	Hydrogen content* [mol H/cm <sup>3</sup> ]
Fe	7.874	55.845	0.141	-
Fe(OH) <sub>2</sub>	3.4	89.859	0.0378	0.0756
H <sub>2</sub> O at 25°	0.997	18.015	0.0553	0.111
KOH		56.106		
Electrolyte: 25 wt% KOH solution at 25°	1.234	-	H <sub>2</sub> O: 0.0514 KOH: 0.0055	0.108

\*) The volumetric hydrogen content is calculated by dividing the density by molar weight and by multiplication with the number of hydrogen atoms. Concerning electrolyte: the hydrogen content is calculated by splitting up the density to 75% Water and 25% KOH. The sum of both is depicted in the table above. Note, there is hardly any variation in hydrogen content between water and electrolyte (25wt% KOH electrolyte).

Table S4 indicates that the density of iron is higher than the density of iron hydroxide. In the case of iron hydroxide 0.0378 moles are present per cm<sup>3</sup>, in the case of iron 0.141 moles. The reduction of 1 cm<sup>3</sup> of iron hydroxide to iron will create a free space of 0.732 cm<sup>3</sup> ( $=1-0.0378/0.141$ ) which will be filled with electrolyte. In the case that 100 % iron hydroxide will be converted to iron, the volume will contain 0.0756 mol H/cm<sup>3</sup> before conversion, and will contain 0.079 mol H/cm<sup>3</sup> ( $=0.732 \times 0.108$  mol H/cm<sup>3</sup>) after conversion to iron. Hence, the background will slightly increase with charging and decrease with discharging.

The following calculation is based on the initial porosity of 64.3%, of the sample. 35.7% of the sample volume is occupied by iron and equal to an iron fraction of 1. The volumetric ratio of iron hydroxide to iron is: 3.73 ( $=0.141/0.0378$ ).

## Extended Experimental Section

Table S5 depicts the calculated relative hydrogen content for the transitions to charging. During the first transition (measurements 31-35) a reduction of background of 5.7% may be expected, during the second transition (measurements 70-73) a reduction of 5.4%. The transitions around measurements 148-154 and 257-264 represent the zone where the fractions of iron and iron hydroxide increase together. A reduction of background occurs here too, in the first transition around 3.3%, in the second transition around 4.7%.

**Table S5. Calculated Relative Hydrogen Content for Transition to Charging**

Spectrum	Fraction Fe [-]	Fraction Fe(OH) <sub>2</sub> [-]	Space Fe [-]	Space Fe(OH) <sub>2</sub> [-]	Free space* [-]	Hydrogen content [-]
31	0.423	0.360	0.151	0.479	0.370	0.0762
35	0.497	0.394	0.177	0.524	0.298	0.0719
70	0.439	0.365	0.157	0.486	0.357	0.0753
73	0.490	0.413	0.175	0.550	0.275	0.0713
148	0.429	0.367	0.153	0.489	0.358	0.0756
154	0.478	0.381	0.171	0.507	0.322	0.0731
257	0.435	0.312	0.155	0.416	0.429	0.0778
264	0.485	0.352	0.173	0.469	0.358	0.0741

\*) The calculation is based on the assumption that the free space is filled with electrolyte with its belonging hydrogen content.

Table S6 depicts the calculated relative hydrogen content for the transitions to discharging, during the first transition (measurements 1-6) an increase of background of 2.9% may be expected, in the second transition (measurements 51-55) an increase of 3.5% and in the third transition (measurements 90-95) an increase of 3.8%.

**Table S6. Calculated Relative Hydrogen Content for Transition to Discharging**

Spectrum	Fraction Fe [-]	Fraction Fe(OH) <sub>2</sub> [-]	Space Fe [-]	Space Fe(OH) <sub>2</sub> [-]	Free space* [-]	Hydrogen content [-]
1	0.678	0.238	0.242	0.317	0.441	0.0716
6	0.617	0.243	0.220	0.323	0.456	0.0737
51	0.674	0.283	0.241	0.376	0.383	0.0698
55	0.608	0.283	0.217	0.377	0.406	0.0724
90	0.674	0.285	0.241	0.380	0.380	0.0697
95	0.602	0.285	0.215	0.379	0.406	0.0725

\*) The calculation is based on the assumption that the free space is filled with electrolyte with its belonging hydrogen content.

The detector counts include the reflections associated with the phase fractions and the incoherent background caused by the samples holder. The distinction in detector counts, which part counts to coherent scattering and incoherent sample holder background and which part counts to hydrogen content is not included in the calculation, hence the previously reported hydrogen related changes form an upper limit for the observed changes. The observed changes are below the calculated changes.

## Results

The following results will be clustered into: (1) Start of Discharging from a Charged Electrode, (2) Steady-state Discharging at the First Plateau (3) Charging a Discharged Electrode from the First Discharge Plateau and (4) The Second Iron Discharge-Plateau.

### Start of Discharging from a Charged Electrode

The executed program contains four transitions from charging to discharging. Three of them were observed by neutron diffraction: (1) from initial floating charge to discharging at 200 mA at the start, (2) from charging at 300 mA to discharging at 300 mA around pattern 52 and (3) the transition from charging at 300 mA to discharging at 200 mA around pattern 91. Patterns 2, 52 and 91 are rest steps, before charging is programmed, thereafter discharging. Figure S6 shows a magnification of the areas of interest. General trends described as gradients and detector count changes can also be seen in Figure 6 (main document).

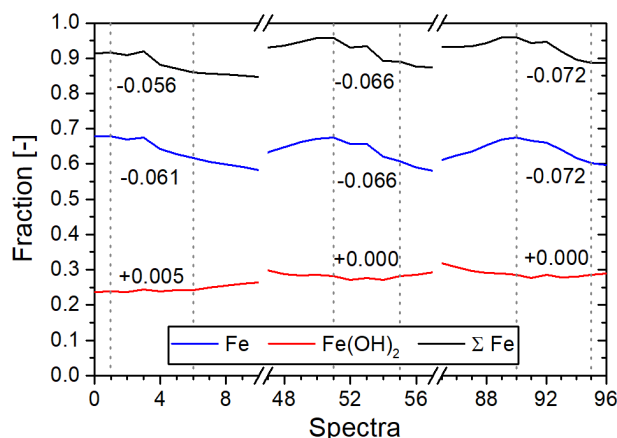


**Figure S6.** Derived normalized molar fractions for the transition from charging to discharging. The change in iron fractions is evaluated between measurements [1-6], [51-55] and [90-95], starting one measurement before rest and ending when steady state rates are reached.

The measured total amount of iron decreases during these transitions between 5.6% and 7.2%, as shown. The decrease is caused by the diminishing of the iron metal fraction, which is about twice as high as expected from stoichiometric electrochemical reactions. This iron decrease is not matched by a corresponding increase of the iron hydroxide fraction. The iron hydroxide fraction shows very little change. The transition is accompanied by an increase of detector counts of about 2%, evaluated after rest between pattern [3-6], [53-55], and [93-96]

## Results

### Steady Gradients for the First Discharge Plateau

Steady state gradients for a discharge rate of 200 mA can be evaluated between pattern [6-29/30], [95/94-117/118] and between [192-204/202], for a discharge rate of 300 mA between pattern [54-68]. Table 2 provides the derived gradients including the deviations from the expected values. The calculated gradients are included in Figure 6, see index linear fit.

**Table S7. Evaluated Fractional Change for Discharging the Iron Electrode, Absolute [-/h] and Relative [%] Compared to a 2-Electron Exchange Process.\***

Fractional change/ rate and pattern	Fe [-/h]/[%]	Fe(OH) <sub>2</sub> [-/h]/[%]
200 mA [6-30/29]	-0.0299/-5.6	0.0214/-32.3
300 mA [54-68]	-0.0486/+2.2	0.0289/-39.1
200 mA [95/94-117/118]	-0.0288/-9.2	0.0204/-35.7
200 mA [192-204/202]	-0.0231/-27.2	0.0235/-25.7

\*) Values between square brackets evaluated pattern; before hyphen: starting pattern, after: end pattern; if slash present: before slash: iron, after: iron hydroxide.

The calculated fractional changes for iron are in good agreement with the expected charges from electrochemical calculations for a two-electron process. At a rate of 200 mA, the change is the 5.6% too slow in cycle 1 and 9.2% too slow in cycle 2. At a rate of 300 mA, the derived change is 2.2% faster than expected. The rates of iron hydroxide formation are about 35% slower than calculated for a two-electron process. The bottom row represents values with starting pattern 192, the first pattern of the second long measurement which starts with a partially discharged electrode. Here both rates are approximately equal, and both are about 25% slower than expected for a two-electron process.

### Charging from the First Discharge Plateau

The transition from discharging to charging at the first plateau can be seen around pattern 31 and 70, with a rest period before charging. In both cases the charging current was 300 mA. The discharging current was set to 200 mA in the first cycle and to 300 mA at the second cycle. Figure S7 shows the derived fractions for iron and iron hydroxide for this transition zone.

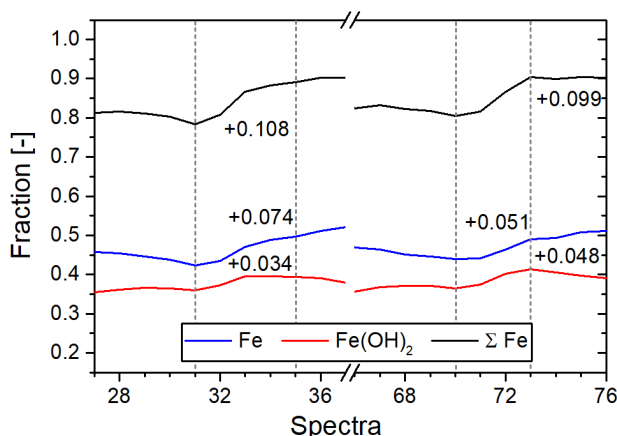


**Figure S7:** Derived normalized molar fractions for the transition from discharging to charging. The change in iron fractions is evaluated between pattern [31-35], and [70-73], starting with the patterns at rest and ending were steady gradients occur.

## Results

The iron hydroxide fraction has a local maximum at patterns 29 and 68. Both measurements are before the rest period. We see a local minimum at the rest period. With charging immediately after the rest period, a significant increase of iron hydroxide is measured. In the first transition we saw +3.4%, in the second transition we saw +4.8%. This is surprising, as the fraction of iron hydroxide is expected to decrease while charging. Constant decreasing gradients can be observed later on, starting with pattern 36 and 73.

At the same time as the increase in iron hydroxide, we observe a substantial increase of the iron fraction. In the first transition the increase was +7.4%, and in the second transition it was +5.1%. In both cases, the determined change is more than twice as high as the change of about 0.8% per measurement that was expected based on the applied electrochemical rate. From pattern 34 and 73 on continuous gradients are observed.

The total amount of detected iron increases with 10.8%, and 9.9%, respectively. This substantial increase is accompanied by a decrease in detector counts of 3% during the first transition, and 4% during the second transition.

After this initial decrease in background, only linear changes in fractions were observed. Table 3 shows the derived fractional changes for charging the iron electrode. Interestingly, two gradients concerning the iron fraction can be derived. The first gradient lags behind the expected phase change, by 5.8% and 22.9%. The second gradient, towards the end of the charging cycle, exceeds predicted values by +8.0%, and +16.4%.

**Table S8. Evaluated Fractional Change for Charging the Iron Storage Electrode, Absolute [-/h] and Relative [%] Compared to a 2-Electron Exchange Process.\***

Fractional change/ rate and pattern	Fe [-/h]/[%]	Fe(OH) <sub>2</sub> [-/h]/[%]
300 mA [34/36–47/49]	0.0448/-5.8	-0.0331/-30.2
300 mA [47-50]	0.0513/+8.0	
300 mA [73-82/88]	0.0366/-22.9	-0.0329/-30.8
300mA [82-89]	0.0553/+16.4	
300 mA [281-284]	0.0507/+6.7	-0.0274/-42.4

\*) Values between square brackets evaluated pattern; before hyphen: starting pattern, after: end pattern; if slash present: before slash: iron, after: iron hydroxide.

The increase in iron fraction fades out at the end of the charging process (see Figure 6 and 7). At the end of charging, the voltage reaches a stable value. This indicates that hydrogen formation has become the dominant process, see SI, Figure S3.

For iron hydroxide, one gradient can be derived for each charge cycle. In both cases the expected fractional change lags behind, the expected change for a two electron process at the applied rate, by 30.2% and 30.8% respectively. The decrease of the iron hydroxide fraction nearly stops towards the end of the charging process, in both cases three pattern, pattern 49 and 88 before the rest steps, pattern 52 and 91 respectively (see Figure 6 and 7).

The final patterns, 281 to 284, show the charging process close to hydrogen evolution, however, no stable voltage is reached yet. The derived rates are in line with previous observations, the increase in iron fraction is 6.7% above expectation while iron hydroxide stays behind by 42.4%.

The voltage profile, Figure 6 and SI Figure S3, shows a similar behavior during the charging process. First a steep increase is seen, followed by a steady voltage increase. Towards the end of the charging process the voltage increases again, and then finally flattens out.



## Results

### The Second Iron Discharge-Plateau

FeOOH is detected in measurements 119-149 and 203-257. Outside these boundaries, the detected fraction of FeOOH seems more like noise. It can be observed that the amount of iron remains constant while FeOOH is present, so iron is inactive/passivated at this stage. With the start of the formation of FeOOH, iron hydroxide is at the maximum of a broad peak, showing a transition zone of roughly 6 measurements or about 1.5 hours of discharge time.

During the second discharge plateau, the decrease of the iron hydroxide phase fraction is steadily increasing, see Figure 6. Table S9 provides an overview of the average fractional decrease during the applied different discharge rates, as well as the rate at the beginning and at the end of each rate step.

**Table S9. Evaluated Fractional Change for Fe(OH)<sub>2</sub> while Discharging the Iron Storage Electrode, Absolute [-/h] and Relative [%] Compared to a One-Electron Exchange Process. \***

Fractional change/ rate and pattern	Begin [-/h]/[%]	Average [-/h]/[%]	End [-/h]/[%]
200 mA [124-133]	-0.0260 / -58.9	-0.0317 / -50.0	-0.0444 / -29.9
100 mA [135-138]		-0.0189 / -40.3	
150 mA [209-218]	-0.0101 / -78.7	-0.0182 / -61.6	-0.0279 / -41.3
100 mA [220-242]	-0.0179 / -43.3	-0.0246 / -22.3	-0.0312 / -1.6

\*) Values between square brackets evaluated pattern; before hyphen: starting pattern, after: end pattern

The table above indicates that the derived rates are lower than expected. Only at the end of the last discharge step is the decrease of Fe(OH)<sub>2</sub> as fast as expected. The steady increase in curvature makes the fractional changes derived for the second discharge, at a discharge current of 100 mA, exceed the fractional changes derived for a discharge current of 150 mA. Because of this, the deviation from expectations is reduced by about 40% points.

The derived fractional changes for the formation and the reduction of FeOOH are delayed compared to the calculated values for a one electron exchange process, see Table S10. During the second deep discharge, the rates are in better agreement, for formation they are 30.2% too low, and for the reduction 20.4% too low. The rates for the formation of Fe(OH)<sub>2</sub> are even slower, in both cases about 60% too low.

**Table S10. Evaluated Fractional Change during Examination of the Second Iron Discharge Plateau, Absolute [-/h] and Relative [%] Compared to a One-Electron Exchange Process. \***

Fractional change/ rate and pattern	FeOOH [-/h]/[%]	Fe(OH) <sub>2</sub> [-/h]/[%]
200 mA [120-134]	-0.0315/-50.3	
100 mA [135-140]	-0.0124/-61.0	
300 mA [140/141-149/148]	0.0631/-33.6	-0.0378/-60.2
100mA [208-245]	-0.0221/-30.2	
300 mA [245-257]	0.0756/-20.4	-0.0376/-60.4

\*) Values between square brackets evaluated pattern; before hyphen: starting pattern, after: end pattern; if slash present: before slash: iron oxyhydroxide, after: iron hydroxide.

## Results

Both phases, FeOOH and Fe(OH)<sub>2</sub> show a clear transition point when switching from discharging to charging. With additional charging FeOOH disappears and then the iron fraction starts increasing. Remarkably, both phases, Fe and Fe(OH)<sub>2</sub> increase then simultaneously, during the first deep discharge for about 5 patterns, during the second deep discharge for about 7 patterns. So conversion of Fe<sup>2+</sup> to Fe and conversion of Fe<sup>3+</sup> to Fe(OH)<sub>2</sub> take place. Notably, during patterns 258 and 262 we have close to perfect agreement, between measured fractional change and electrochemical charge input when assigning 66% of the charge contribute the formation of Fe in a 2-electron process and 29% of the charge to the formation of Fe(OH)<sub>2</sub> in a 1-electron process.

This increase in crystalline iron content can be seen in Figure 6, the middle of which shows the total detectable (crystalline) iron content. The iron content stays constant within the model including FeOOH during deep discharging. So the decrease in Fe(OH)<sub>2</sub> is compensated by the formation of FeOOH. On charging, the decrease of FeOOH is faster than the increase in Fe(OH)<sub>2</sub>, so the total detectable iron content drops, by about 4% and 7%, respectively for the first and second deep discharge. The total detectable iron content reaches a minimum when FeOOH disappears. With further charging the measureable crystalline iron content increases by about 10% until measurement 167 after for the first deep discharge, and by about 13% until measurement 284 after the second deep discharge.

### Correlation between Phase Precipitation and Detector Counts

The mechanism of phase precipitation and dissolution may explain the massive changes in the transition zones. At the start of the discharge period, a substantial amount of crystalline iron disappears while no detectable iron hydroxide is formed. The porosity inside the electrode increases, and with it, the amount of electrolyte inside of the electrode. The calculation indicates an increase in hydrogen content inside the sample for these three transitions of: +2.9% for pattern 1-6; +3.5% for pattern 51-55; and +3.8% for pattern 90-95. At the start of charging, a substantial amount of iron and iron hydroxide forms and the porosity inside the sample decreases, and with it, the amount of electrolyte in the electrode. The calculation indicates a decrease in hydrogen content of: -5.7% for pattern 31-35; and -5.4% for pattern 70-73. A substantial decrease in counts, but with a wider spread, can be observed the two times when both iron and iron hydroxide fractions increase simultaneously, after iron oxyhydroxide has disappeared. In the first case, pattern 148-154, the calculation indicates a decrease of 3.3% of hydrogen content, in the second case, pattern 257-264, a decrease of 4.7%. Hence, it is likely that, here too, phase precipitation causes electrolyte displacement as well as with a reduction in detector counts. The speed of change for the detector counts is correlated with the speed of phase precipitation/dissolution.

## Discussion

### Correlation Fractional Phase Changes - Detector Counts

In the regions just after the transitions from charge to discharge or discharge to charge one observes larger/lower changes than can be justified from the electrochemical conversion of solid phases. This may indicate that the screening of the sample by the incoherent scattering of hydrogen varies sufficiently to have an impact on the measured diffraction patterns. The most straightforward explanation would be that the electrolyte content inside the observed sample varies, and that the electrolyte that flows in the beam then screens part of the diffraction intensities.

We have several options to check whether varying hydrogen concentration correlates with diffraction intensities:

(1) Figure 8 shows phase changes and detector counts during discharging. In the transition zone, the detector counts increase by about 1.5% points. During this same period, metallic iron content decreases too fast and the iron hydroxide content remains stable. This could indicate a correlation. However, on continued discharging, the detector count during C1 increases by an additional 4.5% points. Likewise, during C2 the total counts increased by an additional 3.5% points before they flattened out, without any correlation. It seems unlikely that a change of 1.5% causes correlation while a change of 4.5% does not.

(2) Figure 9 shows phase changes and detector counts during charging. In the transition zone the detector counts decrease with 2% (C1) and 5% (C2) until they reach stable values while metallic iron and iron hydroxide increase. In the case of C1 it requires one measurement until the detector counts stabilize while it takes 4 measurements until the iron hydroxide fraction starts declining. In the case of C2 it takes two measurements until iron hydroxide starts declining while it takes four measurements until the detector count is stabilized. At the end of charging, the detector counts for C1 decrease by another 2% while they hardly decrease for C2. Both charging periods show similar behavior for the metallic iron and the iron hydroxide fraction. No clear correlation between detector counts and fractional change can be determined.

(3) A widely distributed decrease in counts is seen while recharging from the second iron plateau, after measurements 148 and 257. Figure 6 and Figure 10 show steady gradients for metallic iron and iron hydroxide. Both measurements show the same pattern of behavior: After FeOOH has vanished, both the iron and the iron hydroxide phases are increasing at the same time. The detector counts stabilize when iron hydroxide starts decreasing. Here it is likely that the change in porosity caused by solid phase precipitation reduces the hydrogen content. However, it is unlikely that the change in background affects the steadily changing phase fractions.

(4) Figure S8 depicts the observed intensities for patterns 71 to 73. These were the three measurements where the highest reduction of detector counts was observed. Slightly increasing intensities for iron and iron hydroxide were observed, consistent with the notion of both amorphous  $\text{Fe}^{2+}(\text{OH})_2$  and amorphous  $\text{Fe}^{3+}\text{OOH}$  being reduced forming crystalline Fe and  $\text{Fe}(\text{OH})_2$  respectively, while the background - together with the two Ni reflections - substantially decreases. The insert shows the data with the background subtracted, confirming an increase of the intensities of metallic iron and iron hydroxide while the intensities for nickel remain stable.

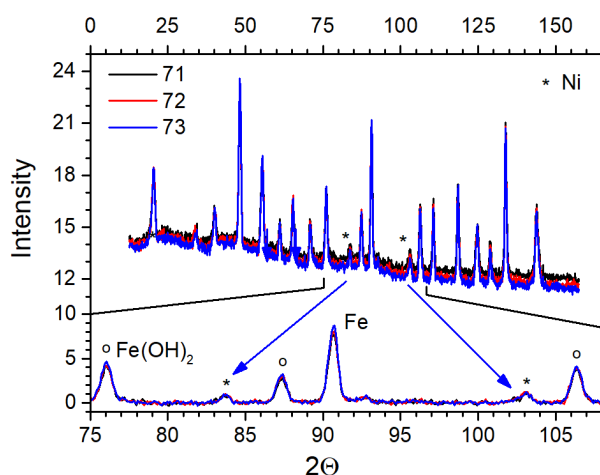


**Figure S8.** Top: Observed stable intensities with decreasing background for pattern 71-73 (the first three charging pattern after rest). The two Ni dominated reflections are marked with a \* and shift together with the background. Bottom: magnification for a  $2\Theta$  range from 75 to 108 degrees, data with the background subtracted.

We conclude that correlation between the changes in the phase fractions and detector counts exists when changes in the detector counts can be expected due to phase precipitation. No correlation is present when changes in detector counts occur due to gas accumulation/release. Hence, it is unlikely that changes in the background intensities affect the sample screening.

Even with correlation, the main findings of current work would not change: the high amount of iron hydroxide is already high initially, and accumulates further upon first plateau operation; the absence of substantial amounts of crystalline iron phases indicates the presence of iron in an amorphous phase; simultaneous precipitation of metallic iron and iron hydroxide occurs, indicating the presence of an amorphous iron (II) phase and an amorphous iron (III) phase; and the identification of  $\delta$ -FeOOH as iron phase for the second discharge plateau.

## References

1. Toby, B.; B. Von Dreele, R., GSAS-II: The Genesis of a Modern Open-Source All-Purpose Crystallography Software Package. *Journal of Applied Crystallography* **2013**, *46*, 544-549.
2. Quirós, M.; Gražulis, S.; Girdzijauskaitė, S.; Merkys, A.; Vaitkus, A., Using SMILES strings for the description of chemical connectivity in the Crystallography Open Database. *Journal of Cheminformatics* **2018**, *10* (1), 23.
3. Gražulis, S.; Chateigner, D.; Downs, R. T.; Yokochi, A. F. T.; Quiros, M.; Lutterotti, L.; Manakova, E.; Butkus, J.; Moeck, P.; Le Bail, A., Crystallography Open Database - an open-access collection of crystal structures. *Journal of Applied Crystallography* **2009**, *42* (4), 726-729.
4. Gražulis, S.; Daškevič, A.; Merkys, A.; Chateigner, D.; Lutterotti, L.; Quirós, M.; Serebryanaya, N. R.; Moeck, P.; Downs, R. T.; Le Bail, A., Crystallography Open Database (COD): an open-access collection of crystal structures and platform for world-wide collaboration. *Nucleic Acids Research* **2011**, *40* (D1), D420-D427.
5. Gražulis, S.; Merkys, A.; Vaitkus, A.; Okulic-Kazarinas, M., Computing stoichiometric molecular composition from crystal structures. *Journal of Applied Crystallography* **2015**, *48* (1), 85-91.
6. Merkys, A.; Vaitkus, A.; Butkus, J.; Okulic-Kazarinas, M.; Kairys, V.; Gražulis, S., COD::CIF::Parser: an error-correcting CIF parser for the Perl language. *Journal of Applied Crystallography* **2016**, *49* (1), 292-301.
7. Downs, R. T.; Hall-Wallace, M., The American Mineralogist crystal structure database. *American Mineralogist* **2003**, *88* (1), 247-250.
8. Aroyo, M. I.; Perez-Mato, J. M.; Capillas, C.; Kroumova, E.; Ivantchev, S.; Madariaga, G.; Kirov, A.; Wondratschek, H., Bilbao Crystallographic Server: I. Databases and crystallographic computing programs. *Zeitschrift für Kristallographie - Crystalline Materials* **2006**, *221* (1), 15-27.